minerals

MDPI

Article

Microstructural Relationship between Olivine and Clinopyroxene in Ultramafic Rocks from the Red Hills Massif, Dun Mountain Ophiolite

Yilun Shao [1,2,*], Marianne Negrini [2], Cai Liu [1] and Rui Gao [3]

[1] College of Geoexploration Science and Technology, Jilin University, Changchun 130026, China
[2] Department of Geology, University of Otago, Dunedin 9054, New Zealand
[3] School of Earth Science and Engineering, Sun Yat-sen University, Guangzhou 510275, China
* Correspondence: ylshao@jlu.edu.cn

Abstract: The microstructural relationship between olivine and clinopyroxene is significant in recovering the mantle evolution under clinopyroxene-saturated melting conditions. This study focuses on olivine/clinopyroxene-related ultramafic rocks (dunite, wehrlite, olivine clinopyroxenite, and clinopyroxenite) in the Ells Stream Complex of the Red Hills Massif. (Olivine) clinopyroxenites have an A/D-type olivine crystallographic preferred orientation (CPO) whereas peridotites have various olivine CPO types. B-type olivine CPO was newly discovered, which may have been generated under hydrous conditions. The discovery of B-type CPO means that all six olivine CPO types could exist in a single research area. Clinopyroxene CPOs also vary and have weaker deformation characteristics (e.g., lower M index and weaker intracrystalline deformation) than olivine; thus, they probably melted and the clinopyroxene-rich ultramafic bands existed as melt veins. Irregular clinopyroxene shapes in the peridotites and incoherent olivine and clinopyroxene CPOs ($[100]_{OL}$ and $[001]_{CPX}$ are not parallel) also indicate a melted state. The dominant orthorhombic and LS-type CPOs in olivine and clinopyroxene imply that simple shear was the main deformation mechanism. Such complicated microstructural characteristics result from the overprinted simple shear under high temperatures (>1000 °C) and hydrous melting environments until the melt-frozen period. This case study is helpful to better understand the olivine and clinopyroxene relationship.

Keywords: CPO; olivine–clinopyroxene relationship; melting; simple shear

check for updates

Citation: Shao, Y.; Negrini, M.; Liu, C.; Gao, R. Microstructural Relationship between Olivine and Clinopyroxene in Ultramafic Rocks from the Red Hills Massif, Dun Mountain Ophiolite. *Minerals* **2023**, *13*, 1415. https://doi.org/10.3390/min13111415

Academic Editor: Juan Gómez-Barreiro

Received: 23 September 2023
Revised: 3 November 2023
Accepted: 3 November 2023
Published: 6 November 2023

Copyright: © 2023 by the authors. Licensee MDPI, Basel, Switzerland. This article is an open access article distributed under the terms and conditions of the Creative Commons Attribution (CC BY) license (https://creativecommons.org/licenses/by/4.0/).

1. Introduction

Olivine and clinopyroxene are two of the main minerals in ultramafic rocks and can form dunite, wehrlite, olivine clinopyroxenite, and clinopyroxenite in the order of increasing clinopyroxene percentage. Although not as common as orthopyroxene, clinopyroxene is an important mineral in mantle rocks [1–3]. Wehrlite is the most common peridotite with clinopyroxene, which is generated by either a melt-rock reaction or interaction with SiO_2-undersaturated magmas [4–6]. Although the solid second phase may inhibit the development of the olivine crystallographic preferred orientation (CPO) [7,8], wehrlites in different areas and geological environments can generate various olivine CPO types (B, E, and AG-type; [9–11]). In comparison, (010) [001] is the most common clinopyroxene CPO type [12–14] whereas it is not dominant in wehrlite or other peridotite types [15–17]. (Olivine) clinopyroxenites are usually banded or veined in natural outcrops [18–20]. The main generation mechanisms of clinopyroxenites include (1) oceanic basaltic crust recycling by subduction [21–23], (2) basaltic melt crystallization [24,25], and (3) melting and the melt-rock reaction [26,27]. The (010) [001] CPO is common in clinopyroxenites of different generations [14,19,20,24].

As typical mantle peridotites mostly have dominant orthopyroxene as the second phase [28]; dunites with clinopyroxene and wehrlites are much less frequently discovered

in natural outcrops and (olivine) clinopyroxenites are even worse. The microstructural studies between olivine and clinopyroxene are not so common, particularly in natural ultramafic rocks [15,29,30]. As clinopyroxene might experience a melting period, the in situ second phase is either solid or liquid which might determine the final olivine CPO type(s). Similarly, olivine grains are the second phase in olivine clinopyroxenite and clinopyroxenite and their potential influence on clinopyroxene has yet to be discovered. Stress and strain are also important factors influencing olivine and clinopyroxene CPOs [13,30,31]. Without detailed studies on the olivine–clinopyroxene deformation relationship, the potential effects of clinopyroxene during mantle evolution are probably ignored.

The Dun Mountain Ophiolite Belt located in New Zealand has excellent peridotite outcrops that have attracted the attention of many researchers. The Red Hills Massif has many types of olivine/clinopyroxene-dominant ultramafic rocks which supply a valuable natural laboratory to detect the relationship between olivine and clinopyroxene [18,32], with different olivine modal contents. Further microstructural research on the olivine–clinopyroxene relationship is helpful for discovering the ultramafic rock kinematics of mantle evolution.

2. Geological Setting

As part of the Dun Mountain Ophiolite Belt, the Red Hills Massif is 120 km^2, approximately 15 km long and 8 km wide (Figure 1a; [18,33,34]). Subduction initiation occurred during the late Permian; thus, the Ophiolite Belt represents a forearc early mantle wedge environment [32,34–36]. The Dun Mountain Ophiolite Belt is divided into the Lee River Group and Dun Mountain Ultramafics (Figure 1a); the former unit is dominated by sheeted dike complexes (diabase and microgabbro) and massive and pillow basalts while the latter unit is dominated by peridotites and pyroxenites [18,32,37,38].

The Red Hills Massif is located in the northern part of South Island, New Zealand (Figure 1a), and includes Two Tarns Harzburgite, Plagioclase Zone, Plateau Complex, and Ellis Stream Complex, from east to west [32,36]. Clinopyroxene-rich peridotite and (olivine) clinopyroxenite outcrops account for the westernmost Ellis Stream Complex (or Ellis Stream Shear Zone (ESSZ); Figure 1a; [18,36,39]). The equilibrium temperature is normal (~1000 °C) while the pressure is low (0.5 GPa) due to the close proximity to the crustal area [36,39,40]. Rare earth element (REE) data reveal that the complex (equal to the upper unit in [18]) is enriched by the melt-rock reaction and that clinopyroxenites originate from frozen melt [18,32,41].

The volume of dunite is dominant and the olivine grains are equigranular [8,18,42]. The dominant strike direction is along the N-S, with (sub)vertical lineations (Figure 1b). The rock masses are mostly banded whereas clinopyroxenite may have isoclinal folds and irregular channels (Figure 1b; [8]) possibly resulting from overprinting by vertical shear [36,39]. Five of the six typical olivine CPOs (except for the B-type) were discovered in the Ellis Stream Complex which is considered to be the result of multiple geological events and fewer second-phase restrictions [8,36,39,40].

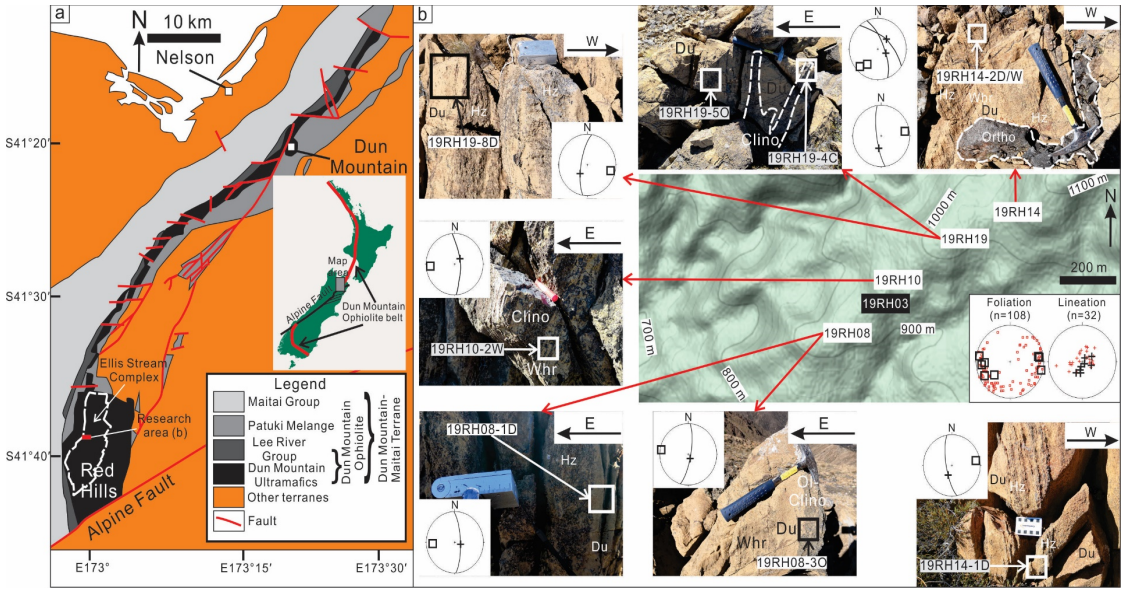


Figure 1. (**a**) Geological map of the northern Dun Mountain Ophiolite Belt located on the north side of Alpine Fault. (**a**) Is modified from [40]. The Ellis Stream Complex area is circled by the white dashed line. (**b**) Google Map topographic image (https://www.google.com/maps/@-41.6435839,172.9998501,15.79z/data=!5m1!1e4?authuser=0&entry=ttu, accessed on 20 October 2023) of the research area (red rectangle in (**a**) and ultramafic rock collection positions (black words with white backgrounds represent positions in this case study, white word with black background represents positions from [8]). Inset represents foliation poles to the plane (black squares) and lineations (black crosses) measured in the sample collection area, plotted in lower hemisphere equal area projections. A stereonet of foliation, foliation pole to plane, and lineation of each sample is shown near or within the photo. White dashed lines in (**b**) show whole folds in the research area. Hz: harzburgite; Du/D: dunite; Whr/W: Wehrlite; Ol-Clino/O: olivine clinopyroxenite; Clino/C: clinopyroxenite; Ortho: orthopyroxenite. Similarly hereinafter.

3. Materials and Methods

3.1. Sample Preparation

Similar to [8], ultramafic samples with less serpentine and prominent grain shapes (particularly olivine and clinopyroxene) were selected. All samples were oriented (thin sections were perpendicular to foliation and (sub)parallel to lineation) with the help of elongated spinel and clinopyroxene grains from peridotites and clinopyroxene-dominant (clinopyroxene > 50%) ultramafic rocks separately [19,43]. Thin sections were polished with $\geq$1 μm diamond followed by colloidal silica [44] and then coated with ~10 nm of carbon. Samples 19RH14-1D, 19RH08-1D, and 19RH19-8D were the same as those of [8] and their clinopyroxene data were added in this case study.

3.2. Electron Backscatter Diffraction (EBSD) Analysis

EBSD analysis was conducted using a Zeiss Sigma VP-FEG-SEM (provided in Otago Micro and Nanoscale Imaging (OMCI), University of Otago, Dunedin, New Zealand) with an accelerating voltage of 30 kV, a beam current of ~100 nA, 2 × 2 binning, a working distance of ~30 mm, and a tilt of 70°. Generally, we conducted analysis by choosing a 50 μm step size for each sample. Raw EBSD data were processed using Channel 5 software noise reduction [45]. Six neighbor extrapolations with iterations were initially applied, followed by wildspike and finally, by five neighbor extrapolations without iteration. Additional noise reduction was performed to prevent the influence of serpentine (see [8] for details). For a statistical view of the magnitude of the internal distortion [46,47] of ultramafic rocks, we used the grain reference orientation deviation (GROD) (or mis-to-mean (M2M) in some studies) parameter to infer intracrystalline plastic deformation. The GROD represents

the average deviation of the orientation of a measurement point from the mean grain orientation [47].

Reconstructed grains were defined using the MTEX toolbox (5.10 version; http://mtex-toolbox.github.io; accessed on 3 September 2023, [48]) with threshold misorientations for grain boundaries of 10° [49]. The grain size (two-dimensional) was calculated as the diameter of a circle equivalent to the grain. Orthopyroxene grain-size data from the harzburgites mentioned by [8] were also measured in this case study to better infer the deformation conditions of clinopyroxene. Similar to [8], as the step size was 50 μm, grains less than 200 μm were not considered in CPO data or grain size statistics in selected ultramafic rocks, to exclude the fine grains. Owing to their minor modal content, orthopyroxene and spinel in the ultramafic samples were not measured. CPO data were presented as one point per grain in lower hemisphere stereographic projections with contours based on a counting cone with a 20° half-width using the MTEX toolbox [50]. If valid grains were less than 100, CPO data were plotted as points (each point represents one grain) with contour outlines.

3.3. M Index and BA/LS Index

The misorientation index (M index) is a measure of CPO strength and is calculated from the random pair misorientation angle distribution [51]. The M index has a value of zero for a uniform distribution and one for a single crystal. The orthopyroxene M index of the harzburgites mentioned by [8] was also calculated. Eigenvalues, derived from the "orientation tensor" method for analyzing directional data [52], enable the characteristics of the CPO in an individual stereogram (e.g., [100]) to be quantified. Vollmer [53] used three eigenvalues (λ1, λ2, and λ3) to define components of the CPO as point (P), girdle (G), and random (R), P = λ1–λ2, G = 2(λ2–λ3), R = 3λ3. Mainprice et al. [54] adapted this approach and defined the BA index to examine olivine CPOs. The BA index uses eigenvalues to discriminate between the axial-[010] (equivalent to AG-type), orthorhombic (equivalent to A–C and E-type), and axial-[100] (equivalent to D-type) olivine CPOs. The BA index has values between 0 and 1 and its formula is $0.5 \times (2 - (P010/(G010 + P010)) - (G100/(G100 + P100)))$. The LS index was also introduced to examine clinopyroxene CPOs and is shown as $0.5 \times (2 - (P010/(G010 + P010)) - (G001/(G001 + P001)))$, as introduced by [55]. These indices were calculated using the MTEX toolbox [54]. Even though the BA/LS index is not the determinant to define CPO, the profile of stereographic projections (e.g., clustered or girdled) is the most important factor to determine CPOs.

4. Results

4.1. General Information and Microstructural Observation

The selected ultramafic rocks contained three dunites (19RH14-1D, 19RH08-1D, and 19RH19-8D), two wehrlites (19RH14-2W and 19RH10-2W), two olivine clinopyroxenites (19RH19-5O and 19RH08-3O), and one clinopyroxenite (19RH19-4C) (Figures 1b and 2, Table 1). Eight selected samples were collected from the Ellis Stream Complex, as described by [8], within the same research area. The sample locations are plotted in Figure 1b. The strikes of the foliations were predominantly along the N-S direction and the lineations were (sub)vertical (Figure 1b). 19RH19-4C was collected one-fold and the other specimens were all collected from bands (Figure 1b). The median olivine grain size decreased with increasing clinopyroxene content (Figure 2) and the average olivine grain size showed a similar tendency (Table 1). Orthopyroxene was no more than 2% and spinel was no more than 3% in any of the samples (Table 1). The grain size ranges of orthopyroxene in harzburgites from [8] were 420–500 μm (average) and 350–470 μm (median), respectively (Table 2).

Petrographic observations showed that the olivine and clinopyroxene grains were euhedral and granular, respectively (Figure 3). The clinopyroxene grains in the dunites were separated by different grain sizes (Figure 3a,b). For wherlites, not only do the clinopyroxene grains become larger but aggregated textures also become more common (Figure 3c,d). Clinopyroxene grains also exist as linear or irregular shapes (Figure 3b,d). The aggregated

clinopyroxene grains became dominant in (olivine) clinopyroxenite with much larger areas (Figure 3e,f). All samples were more or less serpentinized and the grain boundaries were mostly curved with a fraction of straight boundaries. Lamellae were also found in clinopyroxene grains (Figure 3c,e).

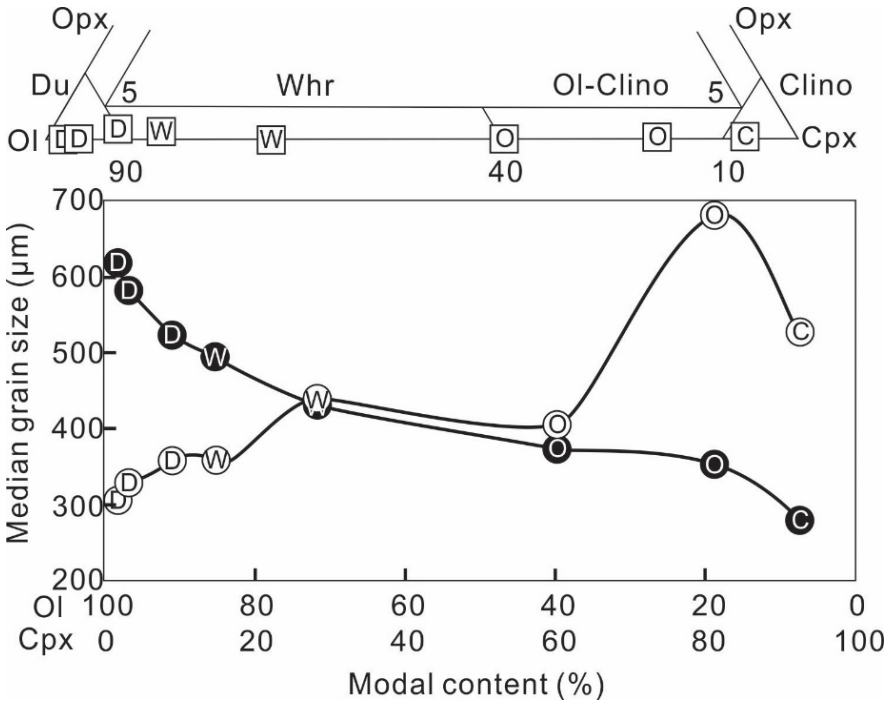


Figure 2. Upper: modal contents of selected ultramafic rocks from the Red Hills Massif; Lower: relationship between olivine/clinopyroxene modal content and median grain size. Black dots: olivine; white dots: clinopyroxene. Similarly hereinafter.

4.2. CPO and SPO (Shape Preferred Orientations) Data

Samples 19RH14-2W, 19RH19-5O, and 19RH08-3O had A-type ((010) [100]) olivine CPO, 19RH19-4C had D-type olivine CPO ({0kl} [100]), and 19RH14-2W had B-type olivine CPO ((010) [001]) (Table 1, Figure 4a,b). The olivine CPOs in the other samples were similar to those reported by [8]. For clinopyroxene, three samples (19RH10-2W, 19RH08-3O, and 19RH19-4C) had traditional (010) [001] CPO, the latter two also had (010) [100] CPO and samples 19RH14-1D and 19RH08-1D had a [001] direction (sub)parallel to the lineation. The $[100]_{CPX}$ of 19RH19-5O was close to the Z direction and the (010) was ~30° in the X direction (Figure 4c). The remaining two samples contained random clinopyroxene CPOs (Figure 4c). Except for 19RH14-1D, 19RH10-2W, and 19RH08-3O, the olivine and clinopyroxene CPOs in the other samples were incoherent (the angle between $[100]_{OL}$ and $[001]_{CPX}$ is more than 20°; Figure 4b,c).

All samples had olivine SPO (sub)parallel to lineation whereas the SPO of clinopyroxene (sub)parallel to lineation occurred in samples with higher clinopyroxene modal content (>50%; $[010]_{CPX}$ in 19RH19-5O, $[001]_{CPX}$ in 19RH08-3O, and 19RH19-4C; Table 1, Figure 4b,c). The remaining samples contained insignificant clinopyroxene SPO (Figure 4c).

Table 1. General and microstructural information of each sample. Samples are in order of increasing clinopyroxene contents. Similarly hereinafter.

Sample No.	Lithology	Ol (%)	Opx (%)	Cpx (%)	Sp (%)	Ol CPO Type	Ol Grain Size (μm)	Ol Grain Median (μm)	Ol M Index	BA Index	Cpx CPO	Cpx CPO Type	Cpx Grain Size (μm)	Cpx Grain Median (μm)	Cpx M Index	LS Index	Ol and Cpx Coherence [a]
19RH14-1D	Dunite	97 (97.6)	0.0	2.3 (2.4)	0.7	D-type	676 ± 589	619	0.2554	0.8276	[001]	SL	309 ± 138	304	0.0643	0.6113	Y
19RH08-1D	Dunite	94.2 (96.9)	0.2	3.0 (3.1)	2.6	C-type	747 ± 486	582	0.1673	0.4937	[001]	SL	371 ± 148	327	0.0689	0.4185	N
19RH19-8D	Dunite	87.6 (91.3)	1.7	8.3 (8.7)	2.4	A–E type	776 ± 678	525	0.1118	0.4426	N/A	SL	408 ± 179	360	0.0077	0.574	N
19RH14-2W	Wehrlite	83.2 (84.6)	1.4	15.1 (15.4)	0.3	A-type	645 ± 485	494	0.2564	0.5766	N/A	S	502 ± 338	358	0.0707	0.2236	N
19RH10-2W	Wehrlite	71.7 (72.2)	0.3	27.6 (27.8)	0.4	B-type	571 ± 412	432	0.1783	0.5404	(010) [001]	SL	639 ± 497	438	0.0675	0.5365	Y (S)
19RH19-5O	Olivine clinopyroxenite	39.8 (40.0)	0.1	59.8 (60.0)	0.3	A-type	460 ± 255	373	0.1211	0.4151	(100) [010]	SL	565 ± 458	405	0.1742	0.6145	N
19RH08-3O	Olivine clinopyroxenite	22.7 (22.7)	0.2	77.1 (77.3)	0.0	A-type	457 ± 287	349	0.1882	0.3205	(010) [001]/[100]	SL	792 ± 536	678	0.103	0.3529	Y (S)
19RH19-4C	Clinopyroxenite	7.3 (7.3)	0.4	92.3 (92.7)	0.0	D-type	390 ± 394	279	0.1497	0.7023	(010) [001]/[100]	S	694 ± 493	528	0.0639	0.1912	N

Ol: olivine; Opx: orthopyroxene; Cpx: clinopyroxene; Sp: spinel. Data in brackets represent modal contents of the olivine-clinopyroxene-only condition. Grain sizes are means and error standard deviations and grain medians are median grain sizes of valid grains. N/A represents random, and the ideal CPO types of clinopyroxene is shown in Figure 5a. [a] Coherency is defined by the angle between $[100]_{OL}$ and $[001]_{CPX}$: coherent ($\leq 10^{\circ}$; Y); sub-coherent (11–20°; Y(S)); and incoherent (>20°; N).

Table 2. Orthopyroxene modal contents and microstructural information of selected harzburgites in [8].

Sample No.	Modal Content (%)	Opx Grain Size (μm)	Opx Grain Size Median (μm)	Opx M Index
19RH14-1H	16.1	471 ± 275	399	0.0928
19RH14-2H	25.5	507 ± 365	351	0.0872
19RH19-8H	17.5	422 ± 281	443	0.0713
19RH19-9H	14.8	454 ± 301	468	0.0696
19RH03-2H	19.4	474 ± 258	463	0.3838
19RH08-1H	19.2	504 ± 313	390	0.1396

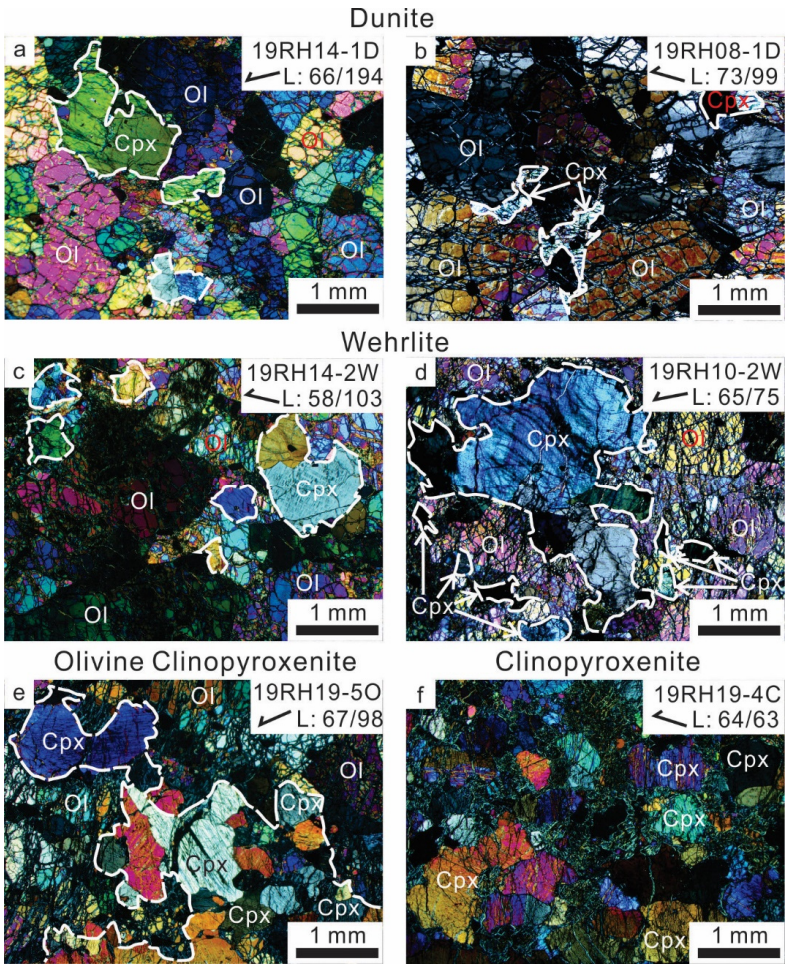


Figure 3. Microphotograph of ultramafic rocks from the research area, clinopyroxene grains or aggregates are circled by white dashed lines (except (**f**)). (**a**) Clinopyroxene grains (coarse- or fine-grained) are enclosed by olivine grains. (**b**) Irregular clinopyroxene grains (fine-grained) within olivine grains. (**c**) Separated and aggregated clinopyroxene grains within olivine grains. (**d**) Aggregated clinopyroxene grains with larger grain size within olivine grains accompanied by irregular single clinopyroxene grains. (**e**) Large aggregated clinopyroxene-grain area within olivine grains. (**f**) Whole-clinopyroxene aggregate with elongated grains in clinopyroxenites. Lamellae can be observed in (**c**,**e**). All microphotographs are xpl and the arrows represent microphotograph directions relative to lineation (L). (**a**,**b**) are dunites, (**c**,**d**) are wehrlites, (**e**,**f**) represent olivine clinopyroxenite and clinopyroxenite, respectively.

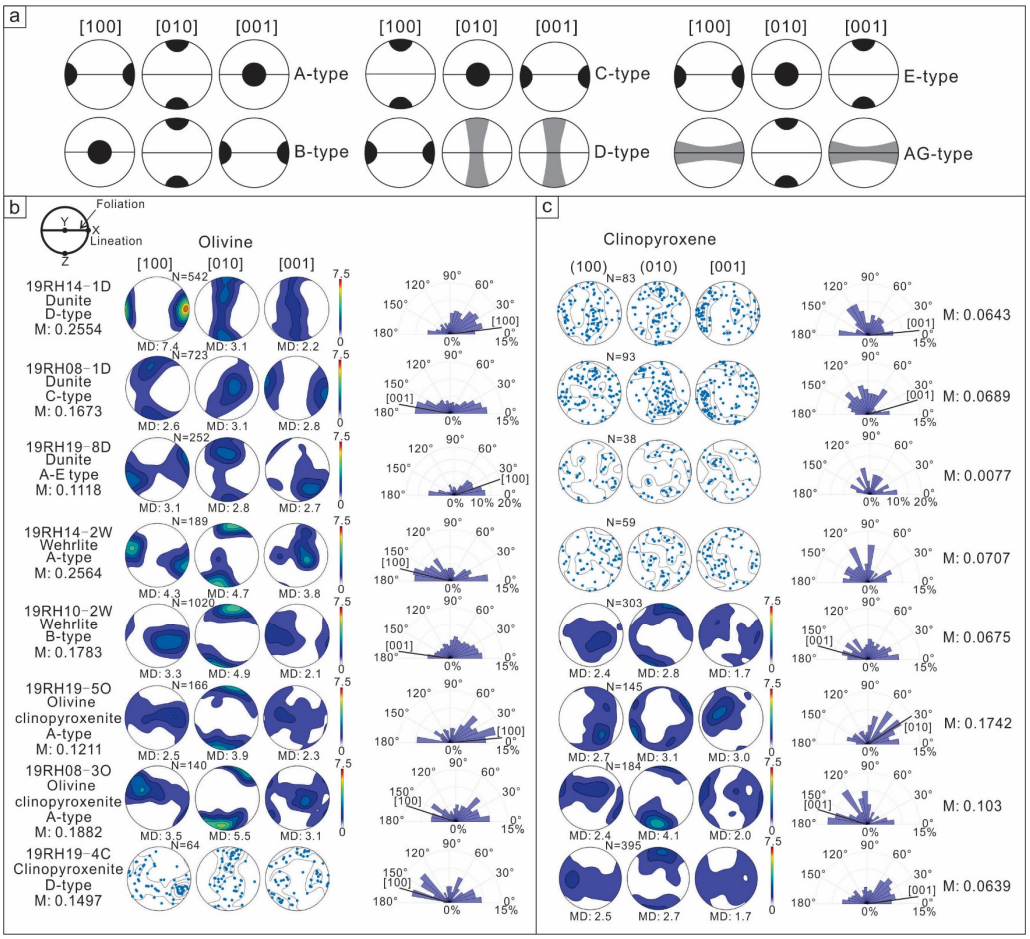


Figure 4. (**a**) Six most typical olivine CPO types (e.g., [56–58]). The E-W direction represents lineation and the vertical E-W plane represents the direction normal to the foliation, modified from [58]. (**b**,**c**) Represent the lower hemisphere and equal area stereographic projections of CPOs of olivine and clinopyroxene in selected ultramafic samples from the Red Hills area, respectively. Foliation and lineation orientations are shown on the left top. N, number of measured grains; MD, maximum density. All the scales are the same (maximum density 7.5). Olivine/clinopyroxene with <100 valid grains are plotted as point and contour outlines, with the same scale. Rose diagrams in (**b**,**c**) represent the distribution of grain long axis orientations (SPO) in the thin section reference frame (0°). Black lines show valid CPO directions in the same reference frame. M represents the M index.

4.3. Other Microstructural Information

The BA index of most samples was higher than 0.35 and the LS index of all samples was lower than 0.65 (Table 1). Four samples were in the 0.35–0.65 range of BA and LS indices (Table 1, Figure 5); thus, orthorhombic olivine CPO and SL-type clinopyroxene CPO are dominant. Generally, the olivine M index was higher than that of clinopyroxene in each sample and the clinopyroxene M index of sample 19RH19-5O was significantly higher than that of the other samples (Figure 5b). Additionally, a comparison of all selected minerals in this case study and [8] showed that the M index of most orthopyroxenes was higher than that of clinopyroxenes and lower than that of olivines (Tables 1 and 2, and Figure 6).

Sample 19RH14-2 had half wehrlite and half harzburgite areas (Figure 7a). The GROD map shows that the internal deformation characteristics (undulatory extinctions and subgrain boundaries) in olivine are more prominent than those in pyroxenes; both orthopyroxene and clinopyroxene are dominated by strain-free (<2°) areas with irregular grain shapes (Figure 7a). In sample 19RH19-5O, the internal deformation characteristics of olivine were also more prominent than those of clinopyroxene (Figure 7b). Intracrystalline deformations (e.g., undulose extinctions, subgrain boundaries, kink bands, etc.) are

also found in different ultramafic rocks (olivine mainly; Figure 7). Although the spinel percentage was low, the spinel grains were uniformly distributed in the ultramafic rocks (Figure 7b).

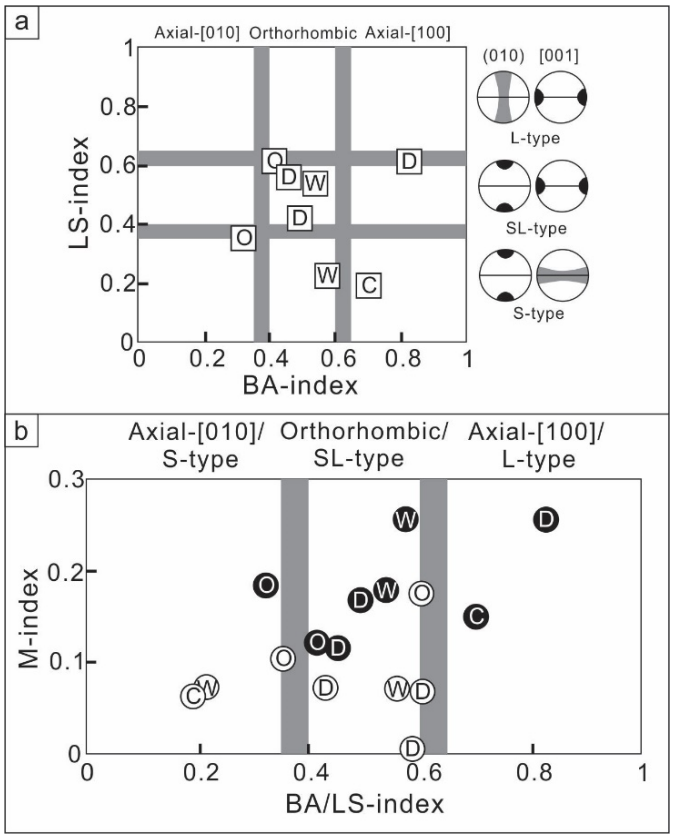


Figure 5. (**a**) Relationship between BA and LS indices of each sample (BA index for olivine, LS index for clinopyroxene). Sketches of stereographic projections represent the ideal conditions for the different ranges of the LS index [20]. (**b**) Relationship between the BA/LS index and M index. Gray areas represent additional orthorhombic/SL-type zones in some studies (e.g., [20,59]).

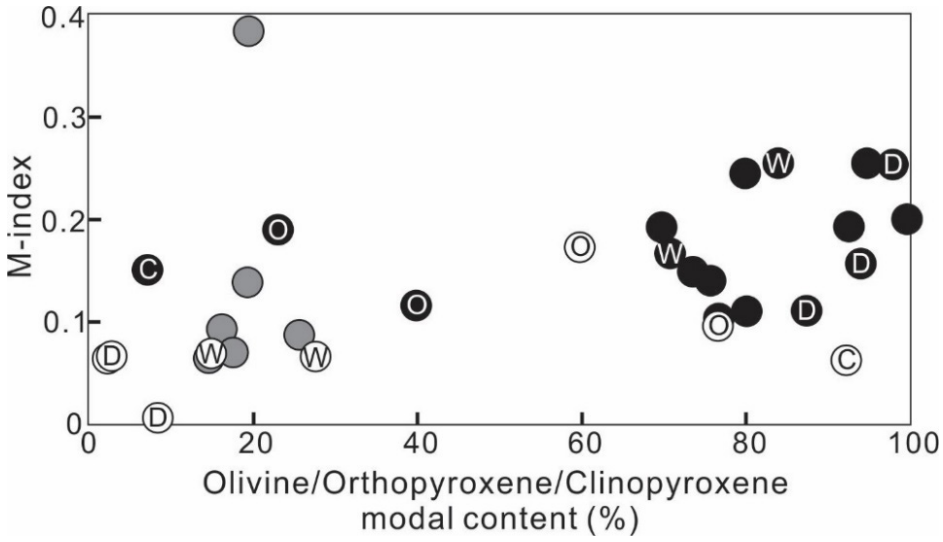


Figure 6. Relationship between olivine/orthopyroxene/clinopyroxene modal content and M index of selected samples in this case study (dots with capital letters) and [8] (dots without capital letters). Gray dots represent orthopyroxene.

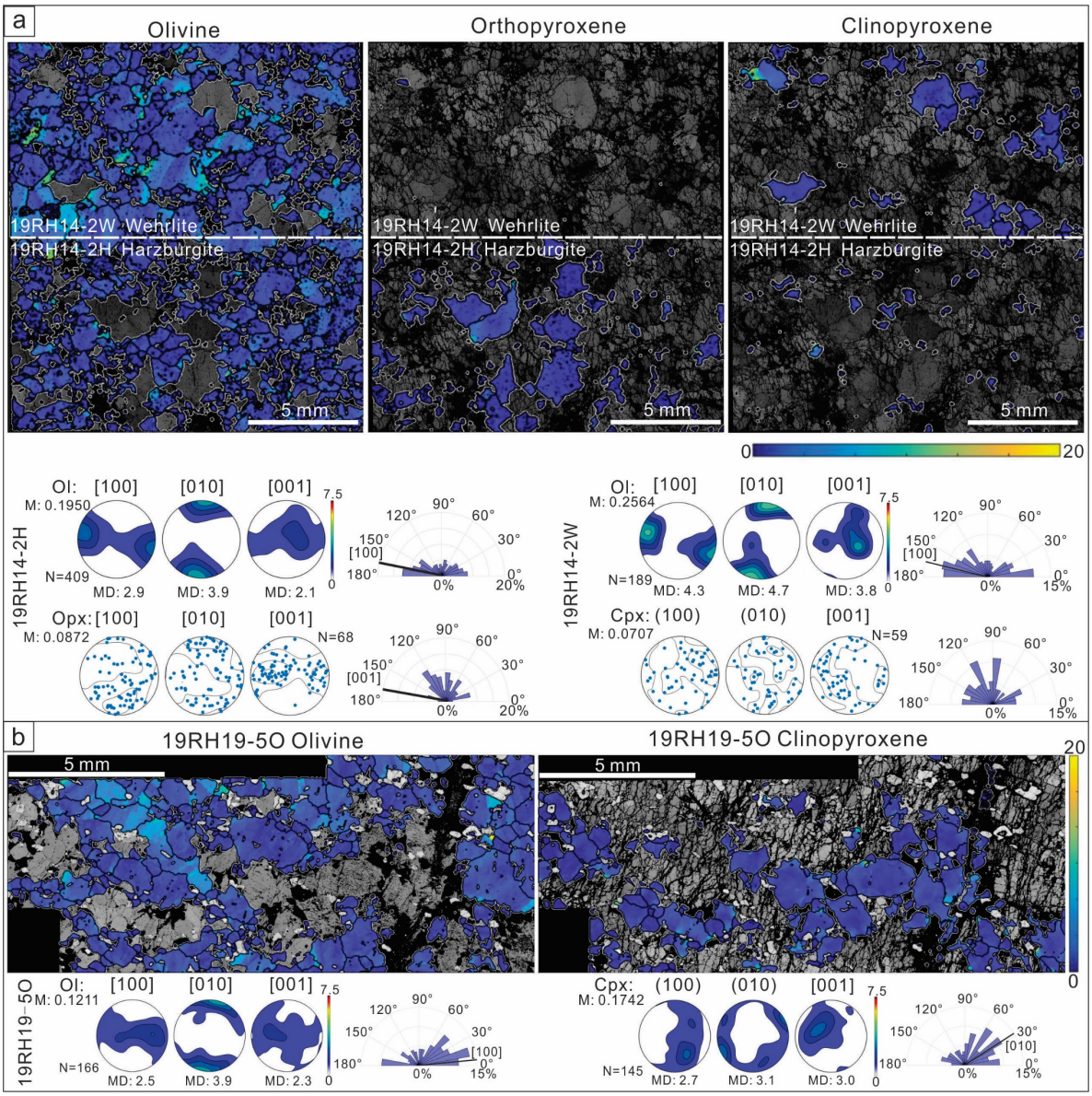


Figure 7. (**a**) Upper: EBSD grain GROD maps of 19RH14-2 over the band contrast map. Wehrlite (19RH14-2W) and harzburgite (19RH14-2H) areas are divided by a bold white dashed line. Lower: olivine and ortho/clinopyroxene CPOs and rose diagrams in wehrlite and harzburgite areas. Rose diagram shown inset represents the SPO distributions of all valid grain long axis orientations in the thin section reference frame (0° is the direction of lineation); the black line shows $[100]_{OL}/[001]_{OPX}$ directions in the same reference frame. Microstructural data of the harzburgite area are all based on [8]. (**b**) Upper: EBSD grain GROD maps of 19RH19-5O over the band contrast map. Lower: olivine/clinopyroxene CPOs and rose diagrams in the olivine clinopyroxenite area. Light gray areas of the band contrast map are spinels. M: M index. Color bars show the angular deviation from mean orientation for olivine, orthopyroxene, and clinopyroxene, with the same scale.

5. Discussion

Similar to [8], the A- and D-types are common in the eastern research area (19RH14 and 19RH19 sample locations; Figure 1b); olivine-dominant samples in the eastern research area (19RH14) have the strongest olivine CPO strength (M index) than other positions (Table 1 of [8] and Table 1 in this study). D-type olivine CPO represents a high-stress condition [31,60]. Additionally, outcrops in the eastern research area have folded clinopyroxenite and orthopyroxenite with low-interlimb angles while clinopyroxenites in the western re-

search area (19RH08, 19RH03, and 19RH10) have homocline bands rather than whole folds (Figure 1b; Figure 3 of [8]). Such characteristics also point to high-stress conditions [60]. Thus, we infer that the eastern research area is influenced by higher stress (high-stress area) than the western area (or low-stress area). The reason why olivine M indexes from 19RH19 are lowest might be due to the fact that initial deformation is minor; the intracrystalline deformations (e.g., Figure 7b) are probably the result of vertical shearing [36,39]. B-type olivine CPO was also discovered in the same research area (Figure 4) of [8]; thus, all six typical olivine CPO types (shown in Figure 4a) exist within a 1-km^2 area. The three samples had typical clinopyroxene (010) [001] CPO and the LS index revealed that SL-type clinopyroxene CPO was dominant. The M index of the clinopyroxene was generally lower than that of the olivine in each sample (except for 19RH19-5O). Unlike olivine, the microstructural characteristics of clinopyroxene are slightly influenced by regional factors (high- or low-stress areas). Sections 5.1 and 5.2 will explore the possible relationship between olivine and clinopyroxene in the microstructural view and Section 5.3 will further elucidate the tectonic evolution in detail. Orthopyroxene data were added to determine the degree of clinopyroxene deformation.

5.1. Identification of Melted Phases during Mantle Evolution

Discovering the detailed melt status is helpful for recovering the mantle kinematics. Both melt-rock reactions and melt flow injection are common during mantle evolution progress [17,20,61–64]. Previous studies in the Red Hills Massif have indicated that the Ellis Stream Complex is influenced by partial melting under high temperature (>1000 °C) conditions [18,32,36,41]. Initially, the harzburgites experienced melt depletion and reactions; the dunites were melt channels and intruded the harzburgites. After the melt channels crystallized, a clinopyroxene-rich melt reaction and re-fertilization occurred.

The addition of the microstructural results recovered the minerals experienced in the melt phase. Generally, the microstructural data (GROD and M index) show that olivine has more prominent deformation characteristics and stronger CPO strength than pyroxenes, regardless of whether it is harzburgite, dunite, wehrlite, or other ultramafic rocks (Figures 5–7). The overall deformation characteristics of orthopyroxene are weaker than those of olivine but stronger than those of clinopyroxene (Figures 6 and 7, Table 2). However, as orthopyroxene in most selected samples and clinopyroxene in five of eight samples have limited valid grains (<150; Figure 4b,c; [8]), the M indexes of orthopyroxene are probably on the high side [51] and the exact orthopyroxene might be similar to clinopyroxene. The GROD maps also revealed that orthopyroxene and clinopyroxene are dominated by strain-free areas, especially in the irregular pyroxene inclusions (Figure 7). 19RH19-5O had the highest clinopyroxene M index, which was even higher than that of olivine, and the strain-free areas were still dominant (Table 1, Figure 7b). Although olivine and clinopyroxene have similar grain shapes and boundaries (Figure 3), once the clinopyroxene content reaches more than 25%, both the average and median grain sizes in clinopyroxene become larger than those in olivine (Table 1, Figure 2). The M index of olivine is usually higher than that of clinopyroxene in each sample (Table 1, Figure 6). Limited valid clinopyroxene grains imply that the exact overall clinopyroxene M indexes might even lower. These characteristics indicate that orthopyroxene and clinopyroxene may be in melt phases [63,65–69]. The random SPO distributions of pyroxenes in ultramafic rocks (Figure 4b,c; Figure 5 of [8]) also imply that they originate from the "crystallized melt".

Even if orthopyroxene and clinopyroxene are melted minerals, they probably underwent different evolution processes. All peridotite outcrops are banded whereas the (olivine) clinopyroxenites are either banded or isoclinic-folded (Figure 1b; [8,32,36]). Modal contents of different ultramafic rocks showed that a certain amount of clinopyroxene (2.9%–4.8%) was found in harzburgite while orthopyroxene in selected ultramafic rocks, in this case study, was minor (<2%; Table 1, Figure 7a). Under petrographic and EBSD observation, small inclusions of pyroxenes were either irregular or linear in shape (Figures 3b,d and 7); orthopyroxene grains were usually separated while clinopyroxene grains were aggregated

(Figure 3c–f; Figure 7b–d of [8]). Both olivine and orthopyroxene inclusions were discovered through microstructural observations (Figure 7; Figure 7d of [8]); however, almost no olivine inclusions were discovered in the clinopyroxene grains (Figures 3 and 7). As orthopyroxene is coherent CPO to olivine [8], it is likely that orthopyroxene was more influenced by mantle kinematics than clinopyroxene. Since clinopyroxene is identified as a melted phase and it existed in peridotites, we infer that the melted clinopyroxene phase injected the peridotite rock mass and both harzburgites and dunite (or later-generated wehrlite) were influenced by clinopyroxene melt percolation.

5.2. Deformation of the Clinopyroxene-Related Ultramafic Rocks

5.2.1. Olivine

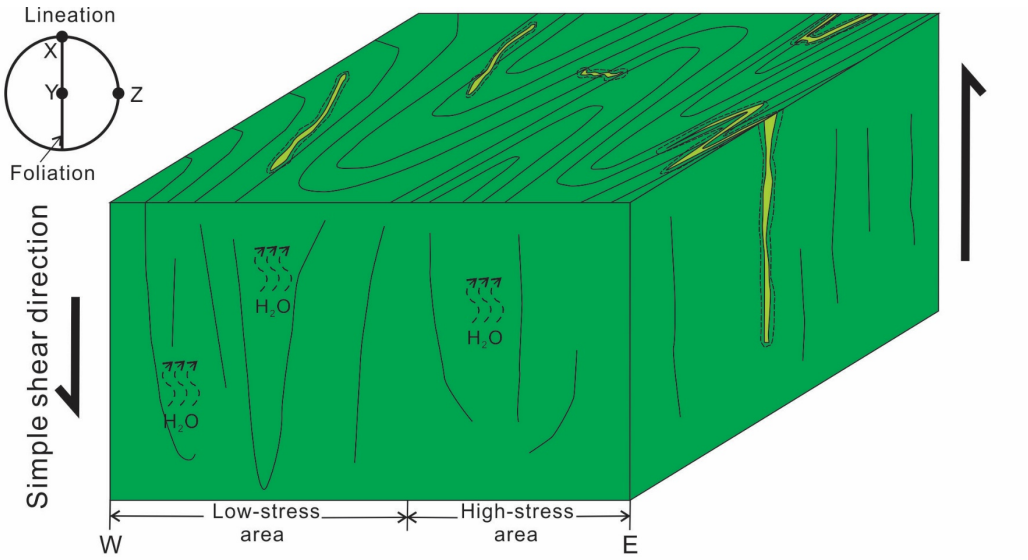
Detailed EBSD data helped us explore the intracrystalline deformation characteristics of the ultramafic rocks, regardless of serpentinization. EBSD GROD maps showed that olivine grains in different ultramafic rocks had prominent intracrystalline plastic deformations (undulose extinctions, subgrain boundaries, and kink bands; Figure 7). Thus, dislocation creep plays a major role in olivine deformation. In comparison, the two pyroxenes were dominated by strain-free areas (Figure 7) and limited intracrystalline deformations were considered to have been generated during the melt crystallization period. 19RH14-2H and 19RH14-2W were close to each other and all had similar A-type CPO and SPO distributions (Figure 7a). Shao et al. [8] reported that harzburgites mostly had an A-type olivine CPO because of the second-phase (orthopyroxene) restriction. Without (or with less) second-phase restriction, peridotites near the harzburgite might have developed other olivine CPO type(s) (the subdivided 19RH19-8D from [8] and this case study). Sample 19RH14-2W retained the A-type olivine CPO which implies that the clinopyroxene-saturated melt was frozen during A-type olivine CPO generation.

As mentioned in [8], the eastern research area has a higher stress than the western research area (Figure 8). The newly-selected ultramafic rocks have similar distribution characteristics; that is, A/D-type CPOs are dominant in the eastern area and CPO types vary (all CPO types except D-type) in the western area (Figures 1b and 4a, Table 1). When the clinopyroxene content was low (<10%), the olivine grains had various CPO types in the different ultramafic samples (Table 1, Figure 4b), regardless of their locations. The two wehrlites had A- and B-type separately. 19RH14-2W, which is located in a high-stress area, was mentioned above.

Another wehrlite, 19RH10-2W, with a newly discovered B-type CPO, was located in a low-stress area. The potential B-type generation mechanisms include a (1) high-water content or mantle wedge-related environment [56,70,71]; (2) diffusion creep in melting condition [72]; (3) GBS with grain size reduction [73]; and (4) high stress or pressure [74,75]. Considering that the research area belongs to the early mantle wedge and experienced hydrous melting [32,36], B-type CPO generation is likely influenced by high water content. Additionally, clinopyroxene-rich bands usually have distinct characteristics (different kinds of folds) from banded peridotites [8] and (olivine) clinopyroxenites are inferred to be involved in melt injection [18], implying that the in-situ geological condition is probably controlled by partial melting. Such an environment might also promote B-type olivine CPO generation because clinopyroxene in wehrlite melts prior to the temperature decrease. Shao et al. [8] mentioned that GBS might be greater in peridotites with solid second phases and finer grain sizes whereas 19RH10-2W has minor grain size reduction characteristics; the second phase (clinopyroxene) was probably melted rather than remaining solid during the olivine CPO generation period. Thus, Hypothesis (3) might not apply to B-type CPO generation. As a result of the finer grain size and pressure, Hypothesis (4) also contradicts the in-situ geological conditions [36,76]. Considering that the research area belongs to the early mantle wedge and has experienced hydrous melting [32,36], the B- and C-type (19RH08-1D) CPO generation probably include high water content [56,70,71].

In the clinopyroxene-dominant samples, olivine had a typical CPO rather than various CPOs (Table 1, Figure 4). The two olivine clinopyroxenites all had A-type CPO and are

located in both high- and low-stress areas. 19RH19-5O has many clinopyroxene aggregates as well as accounting for tiny clinopyroxene inclusions and spinel (light gray areas of the band contrast map) grains (Figure 7b). We inferred that both inclusions and spinel grains inhibited olivine CPO development under high-stress conditions, as mentioned by [8]. In another olivine clinopyroxenite, 19RH08-3O, clinopyroxene was dominant and the olivine still had an A-type CPO which might be due to the low-stress conditions. Only clinopyroxenite is located in the high-stress area and olivine grains had D-type CPO, probably because the aggregates have minor secondary phases.



	Olivine-dominant peridotites (Green)		Clinopyroxene-dominant ultramaifics (Light green)
	Harzburgites	Dunites & Wehrlites	(Olivine) Clinopyroxenites
Low-stress area	Ol: A/AG-type Opx: (100)[001] Ol & Opx CPOs: coherent	Ol: B/C/E-type Cpx: various Ol & Cpx CPOs: coherent or incoherent	Ol: A-type Cpx: (010)[001]/[100] Ol & Cpx CPOs: coherent
High-stress area	Ol: A-type dominant Opx: (100)[001] Ol & Opx CPOs: coherent	Ol: A/D-type Cpx: various Ol & Cpx CPOs: coherent or incoherent	Ol: A/D-type Cpx: various Ol & Cpx CPOs: incoherent

Figure 8. Sketch map of the tectonic evolution of folded ultramafic bands (solid lines) after clinopyroxene-rich melt frozen during the synkinematic period in Ellis Stream Shear Zone (ESSZ; not to scale). Green represents peridotite and light green represents (olivine) clinopyroxenite. The thin dashed lines represent potential melt percolation areas prior to melt cooling down. Dashed lines with arrows represent potential water infiltration. The relative positions (E–W) are also shown. The arrows show a relatively simple shear degree in different positions. Approximate high- and low-stress area ranges (not to scale) are shown at the bottom. The lower text describes the CPO characteristics of olivine and pyroxenes in different rock types and stress areas. Modified from [8].

In summary, 8 of the 17 ultramafic rocks in this case study and [8] had A-type CPO and another 3.5 samples had D-type CPO (the A–D type was counted as 0.5 A- and 0.5 D-type). Type (or orthorhombic) CPO is usually generated under simple shear conditions [56,77] and high-stress simple shear can also generate D-type olivine CPO [31,60]. Additionally, A- and E-type olivine CPOs may coexist under simple shear conditions with similar water contents [78]. The total percentage of A/D/E-type CPOs was 82% (14 of 17 samples). These results imply that simple shear and the related dislocation creep are the primary dynamic mechanisms.

5.2.2. Clinopyroxene

Based on the analysis in Section 5.1, clinopyroxene was considered to be a crystallized melt. The folded structures of the clinopyroxenites in the research area imply that they

took part in the shearing process. As long as the clinopyroxene content is more than 25%, both the average and median clinopyroxene grain sizes become larger than those of olivine (Table 1, Figure 2). However, most samples had a lower clinopyroxene M index than olivine (Table 1, Figures 5 and 6). Sample 19RH19-5O had the highest M index value and both the micrograph and GROD map revealed that subgrains and neoblasts generated by dislocation creep were common whereas strain-free areas were still dominant (Figures 3e and 7b). The main reason for this is that clinopyroxene melted and the main dynamic recrystallization occurred after melt freezing without experiencing pre-melt deformations [65,68]. Olivine in the same sample has a lower M index than clinopyroxene might have due to minor deformation prior to the vertical simple shear (Figure 7b). Additionally, clinopyroxene inclusions in olivine grains had both linear and irregular shapes (Figures 3a–d and 7); thus, partial melting of clinopyroxene occurred until the post-kinematic period [62,79]. Lamellae are not bent by subgrain boundaries which implies that mantle cooling occurred during post-kinematic and static conditions.

Unlike (mostly) coherent olivine and orthopyroxene CPOs in harzburgites (e.g., [8,80]), in the same research area, olivine and clinopyroxene CPOs were usually incoherent (Table 1, Figure 4b,c). This difference was probably due to the two pyroxenes experiencing respective evolutionary progress, as mentioned in Section 5.1. Clinopyroxene-saturated melt occurred during both syn- and post-kinematics, possibly leading to incoherent olivine and clinopyroxene CPOs [17,62,81]. The clinopyroxene-dominant melt veins injected peridotites and became solid and subsequent shearing bent the veins. As the injecting direction might not have been parallel to the solid rock mass and the CPOs of different minerals were not accordant (e.g., plagioclase in residuum and K-feldspar in neosome domain in [68]), such progress might also contribute to incoherent olivine and clinopyroxene CPOs.

In the post-kinematic condition, melted clinopyroxene existed as an irregular shape among the olivine grains, especially in the peridotites (Figures 3a–d and 7). Once crystallized, both CPOs and SPOs were randomly distributed compared with (olivine) clinopyroxenites (Figure 4c). Therefore, peridotites with a minor clinopyroxene content (<25%) had no typical (010) [001] CPO (Table 1, Figure 4c). The three samples had typical clinopyroxene (010) [001] CPO and they all contained accountable clinopyroxene (>25%; Table 1, Figure 4c). Thus, (010) [001] CPO generation was the result of deformation during the synkinematic period and other clinopyroxene CPOs were probably generated by overprinted shearing after melt freezing [8,36,39]. The LS index showed that the SL-type clinopyroxene CPO was dominant (Figure 5). The hypotheses for the origin of the SL-type CPO are (1) pure shear [77], (2) (planar) transition [59,77], and (3) simple shear [31,56]. Pure or simple shear can generate SL-type CPOs whereas pure shear tends to generate clustered (orthorhombic olivine CPOs and SL-type clinopyroxene CPO) rather than girdled CPOs (olivine D/AG-type CPO and S/L-type clinopyroxene CPO) [20,55,82]. Transtension is also one of the generation mechanisms for forming A/D-type olivine CPOs. The research area has decreasing stress from east to west and clinopyroxenes in the western research area (low-stress area) and ultramafic rocks are all SL-type. Previously, we inferred that simple shear is probably the main force in mantle kinematics; such an inference can also be used to interpret the dominant clinopyroxene SL-type CPO. Thus, the most pervasive clinopyroxene SL-type generation mechanism was simple shear.

5.3. Tectonic Evolution Recovery

Based on the above analysis, the tectonic evolution of the Ellis Stream Complex (or ESSZ; [36]) can be better reconstructed (Figure 8). Once the latest simple shear overprinted or partly overprinted the previous structures [36,39], olivine and orthopyroxene CPOs become coherent [8]. As the stress decreases from east to west, the olivine CPO types of peridotites change from dominant A/D-type to various CPO types [8,18]. The clinopyroxene-rich melt was injected into the peridotite massif. Not only do melt channels include olivine-dominant aggregates but melt percolation also occurs with nearby peridotites. The melt-freezing period occurred during simple shearing; thus, the solid-phase

clinopyroxene experienced shearing similar to that of peridotites [20]. Owing to melting conditions, the CPOs of olivine and clinopyroxene are mostly incoherent [17]. With the joining of the melt, either from injection or partial melting and less second-phase restriction, all six olivine CPO types may appear at the same time. Water infiltration may also have contributed to olivine CPO generation.

6. Conclusions

B-type olivine CPO was newly found in the Ellis Stream Complex and the other newly selected ultramafic rocks had an A/D-type olivine CPO. In this case study, the three ultramafic rocks had typical clinopyroxene (010) [001] CPO. Orthorhombic and LS-type CPOs were dominant in olivine and clinopyroxene separately. The olivine and clinopyroxene CPOs were mostly incoherent and the M index of clinopyroxene was generally lower than that of olivine.

Similar to [8], the A- and D-types were dominant in high-stress areas and the low-stress areas had various olivine CPO types. The hydrous melting environment contributed to B-type CPO generation. The weaker deformation characteristics of clinopyroxene are probably due to its melting status. The high-temperature conditions and irregular clinopyroxene-dominant ultramafic bands imply that (olivine) clinopyroxenites were injected into melt veins, which might include olivine aggregates. The nearby peridotites may have been influenced by melt percolation.

Simple shear in a hydrous melting environment is considered the final overprinting deformation force after the clinopyroxene-rich melt veins are frozen. Such kinematics, accompanied by less second-phase inhibition and stress heterogeneity, are likely the dominant mechanisms for generating all six olivine CPO types and the incoherent olivine and clinopyroxene CPOs in the Ellis Stream Complex.

Author Contributions: Conceptualization, Y.S.; Methodology, Y.S.; Software, Y.S. and M.N.; Validation, M.N.; Formal Analysis, Y.S.; Investigation, Y.S.; Resources, M.N., C.L. and R.G.; Data Curation, Y.S.; Writing—Original Draft Preparation, Y.S.; Writing—Review and Editing, M.N. and C.L.; Visualization, Y.S. and M.N.; Supervision, C.L. and R.G.; Project Administration, R.G.; Funding Acquisition, C.L. and R.G. All authors have read and agreed to the published version of the manuscript.

Funding: Financial support for this project is from the "Tectonics of Zealandia" subcontract from GNS, China Scholarship Council (Grant no. 201708250002), and the National Natural Science Foundation of China (Grant no. 41874125, 41972215).

Data Availability Statement: Data are contained within the article.

Acknowledgments: We are grateful to the four anonymous reviewers whose suggestions and comments have notably improved the manuscript. The Reid Helicopters Nelson is thanked for supplying both safe and effective helicopters and the Department of Conservation kindly gave sample collection permission to help us finish this case study. Michael Ofman and Yi Li are thanked for field assistant work. David Prior, James Scott, Eric Stewart, Dushan Jugum, and Stephanie Junior provided useful discussions and significant suggestions. Thanks also to Hamish Bowman for MTEX scripts improvement.

Conflicts of Interest: The authors declare no conflict of interest.

References

1. Smyth, J.; Bell, D.; Rossman, G. Incorporation of hydroxyl in upper-mantle clinopyroxenes. *Nature* **1991**, *351*, 732–735. [CrossRef]
2. Muramoto, M.; Michibayashi, K.; Ando, J.; Kagi, H. Rheological contrast between garnet and clinopyroxene in the mantle wedge: An example from Higashi-akaishi peridotite mass, SW Japan. *Phys. Earth Planet. Inter.* **2011**, *184*, 14–33. [CrossRef]
3. Picazo, S.; Müntener, O.; Manatschal, G.; Bauville, A.; Karner, G.; Johnson, C. Mapping the nature of mantle domains in Western and Central Europe based on clinopyroxene and spinel chemistry: Evidence for mantle modification during an extensional cycle. *Lithos* **2016**, *266*, 233–263. [CrossRef]
4. Ionov, D.; Chanefo, I.; Bodinier, J. Origin of Fe-rich lherzolites and wehrlites from Tok, SE Siberia by reactive melt percolation in refractory mantle peridotites. *Contrib. Mineral. Petrol.* **2005**, *150*, 335–353. [CrossRef]

5. Xiao, Y.; Zhang, H.; Fan, W.; Ying, J.; Zhang, J.; Zhao, X.; Su, B. Evolution of lithospheric mantle beneath the Tan-Lu fault zone, eastern North China Craton: Evidence from petrology and geochemistry of peridotite xenoliths. *Lithos* **2010**, *117*, 229–246. [CrossRef]
6. Marchesi, C.; Konc, Z.; Garrido, C.J.; Bosch, D.; Hidas, K.; Varas-Reus, M.I.; Acosta-Vigil, A. Multi-stage evolution of the lithospheric mantle beneath the westernmost Mediterranean: Geochemical constraints from peridotite xenoliths in the eastern Betic Cordillera (SE Spain). *Lithos* **2017**, *276*, 75–89. [CrossRef]
7. Tommasi, A.; Vauchez, A.; Godard, M.; Belley, F. Deformation and melt transport in a highly depleted peridotite massif from the Canadian Cordillera: Implications to seismic anisotropy above subduction zones. *Earth Planet. Sci. Lett.* **2006**, *252*, 245–259. [CrossRef]
8. Shao, Y.; Prior, D.; Toy, V.; Negrini, M.; Scott, J. Does second phase content control the evolution of olivine CPO type and deformation mechanisms? A case study of paired harzburgite and dunite bands in the Red Hills Massif, Dun Mountain Ophiolite. *Lithos* **2021**, *406*, 106532. [CrossRef]
9. Tommasi, A.; Vauchez, A.; Ionov, D.A. Deformation, static recrystallization, and reactive melt transport in shallow subcontinental mantle xenoliths (Tok Cenozoic volcanic field, SE Siberia). *Earth Planet. Sci. Lett.* **2008**, *272*, 65–77. [CrossRef]
10. Wei, B.; Jin, Z.; Zhang, J. Deformation microstructures and mechanism of ultrahigh-pressure garnet wehrlite from Bixiling, Dabie Mountains. *Earth Sci. -J. China Univ. Geosci.* **2013**, *38*, 983–994, (Chinese with English abstract)
11. Park, Y.; Jung, H. Deformation microstructures of olivine and pyroxene in mantle xenoliths in Shanwang, eastern China, near the convergent plate margin, and implications for seismic anisotropy. *Int. Geol. Rev.* **2015**, *57*, 629–649. [CrossRef]
12. Godard, G.; van Roermund, H.L.M. Deformation-induced clinopyroxene fabrics from ecologites. *J. Struct. Geol.* **1995**, *17*, 1425–1443. [CrossRef]
13. Bascou, J.; Tommasi, A.; Mainprice, D. Plastic deformation and development of clinopyroxene lattice preferred orientations in eclogites. *J. Struct. Geol.* **2002**, *24*, 1357–1368. [CrossRef]
14. Frets, E.; Tommasi, A.; Garrido, C.; Padrón-Navarta, J.; Amri, I.; Targuisti, K. Deformation processes and rheology of pyroxenites under lithospheric mantle conditions. *J. Struct. Geol.* **2012**, *39*, 138–157. [CrossRef]
15. Higgie, K.; Tommasi, A. Deformation in a partially molten mantle: Constraints from plagioclase lherzolites from Lanzo, western Alps. *Tectonophysics* **2014**, *615–616*, 167–181. [CrossRef]
16. Puelles, P.; Ábalos, B.; Gil Ibarguchi, J.; Sarrionandia, F.; Carracedo, M.; Fernández-Armas, S. Petrofabric and seismic properties of lithospheric mantle xenoliths from the Calatrava volcanic field (Central Spain). *Tectonophysics* **2016**, *683*, 200–215. [CrossRef]
17. Chatzaras, V.; Kruckenberg, S.C. Effects of melt-percolation, refertilization and deformation on upper mantle seismic anisotropy: Constraints from peridotite xenoliths, Marie Byrd Land, West Antarctica. *Geol. Soc. Lond. Mem.* **2021**, *56*, 151–180. [CrossRef]
18. Sano, S.; Kimura, J. Clinopyroxene REE Geochemistry of the Red Hills Peridotite, New Zealand: Interpretation of Magmatic Processes in the Upper Mantle and in the Moho Transition Zone. *J. Petrol.* **2007**, *48*, 113–139. [CrossRef]
19. Chin, E.; Soustelle, V.; Liu, Y. An SPO-induced CPO in composite mantle xenoliths correlated with increasing melt-rock interaction. *Geochim. Cosmochim. Acta* **2020**, *278*, 199–218. [CrossRef]
20. Henry, H.; Kaczmarek, M.; Ceuleneer, G.; Tilhac, R.; Griffin, W.; O'Reilly, S.; Grégoire, M.; Le Sueur, E. The microstructure of layered ultramafic cumulates: Case study of the Bear Creek intrusion, Trinity ophiolite, California, USA. *Lithos* **2021**, *388–389*, 106047. [CrossRef]
21. Polvé, M.; Allgre, C. Orogenic lherzolite complexes studied by 87Rb-87Sr: A clue to understand the mantle convection processes? *Earth Planet. Sci. Lett.* **1980**, *51*, 71–93. [CrossRef]
22. Allègre, C.; Turcotte, D. Implications of a two-component marble-cake mantle. *Nature* **1986**, *323*, 123–127. [CrossRef]
23. Lambart, S.; Baker, M.; Stolper, E. The role of pyroxenite in basalt genesis: Melt-PX, a melting parameterization for mantle pyroxenites between 0.9 and 5 GPa. *J. Geophys. Res. Solid Earth* **2016**, *121*, 5708–5735. [CrossRef]
24. Henry, H.; Tilhac, R.; Griffin, W.; O'Reilly, S.; Satsukawa, T.; Kaczmarek, M.; Grégoire, M.; Ceuleneer, G. Deformation of mantle pyroxenites provides clues to geodynamic processes in subduction zones: Case study of the Cabo Ortegal Complex, Spain. *Earth Planet. Sci. Lett.* **2017**, *472*, 174–185. [CrossRef]
25. Zhao, X.; Wang, H.; Li, Z.; Evans, N.J.; Ying, J.; Yang, Y.; Zhang, H. Nature and evolution of lithospheric mantle beneath the western North China Craton: Constraints from peridotite and pyroxenite xenoliths in the Sanyitang basalts. *Lithos* **2021**, *384–385*, 105987. [CrossRef]
26. Ackerman, L.; Jelínek, E.; Medaris, G., Jr.; Ježek, J.; Siebel, W.; Strnad, L. Geochemistry of Fe-rich peridotites and associated pyroxenites from Horní Bory, Bohemian Massif: Insights into subduction-related melt–rock reactions. *Chem. Geol.* **2009**, *259*, 152–167. [CrossRef]
27. Chetouani, K.; Bodinier, J.; Garrido, C.; Marchesi, C.; Amri, I.; Targuisti, K. Spatial variability of pyroxenite layers in the Beni Bousera orogenic peridotite (Morocco) and implications for their origin. *Comptes Rendus Geosci.* **2016**, *348*, 619–629. [CrossRef]
28. Bodinier, J.; Godard, M. Orogenic, ophiolitic, and abyssal peridotites. *Treatise Geochem.* **2003**, *2*, 103–170.
29. Maruyama, G.; Hiraga, T. Grain-to multiple-grain-scale deformation processes during diffusion creep of forsterite+ diopside aggregate: 1. Direct observations: Journal of Geophysical Research. *Solid Earth* **2017**, *122*, 5890–5915. [CrossRef]
30. Zhao, N.; Hirth, G.; Cooper, R.; Kruckenberg, S.; Cukjati, J. Low viscosity of mantle rocks linked to phase boundary sliding. *Earth Planet. Sci. Lett.* **2019**, *517*, 83–94. [CrossRef]

31. Bystricky, M.; Kunze, K.; Burlini, L.; Burg, J. High shear strain of olivine aggregates: Rheological and seismic consequences. *Science* **2000**, *290*, 1564–1567. [CrossRef] [PubMed]
32. Stewart, E.; Lamb, W.; Newman, J.; Tikoff, B. The petrological and geochemical evolution of early forearc mantle lithosphere: An example from the Red Hills Ultramafic Massif, New Zealand. *J. Petrol.* **2016**, *57*, 751–776. [CrossRef]
33. Christensen, N. Structure and origin of the Dun Mountain ultramafic massif, New Zealand. *Geol. Soc. Am. Bull.* **1984**, *95*, 551–558. [CrossRef]
34. Coombs, D.; Landis, C.; Norris, R.; Sinton, J.; Borns, D.; Craw, D. The Dun Mountain ophiolite belt, New Zealand, its tectonic setting, constitution, and origin, with special reference to the southern portion. *Am. J. Sci.* **1976**, *276*, 561–603. [CrossRef]
35. Davis, T.; Johnston, M.; Rankin, P.; Stull, R. The Dun Mountain ophiolite belt in East Nelson, New Zealand. In Proceedings of the International Ophiolite Symposium, Nichoisa, Cyprus, 1–8 April 1979; Cyprus Ministry of Agriculture and Natural Resources: Nicosia, Cyprus, 1980; pp. 480–498.
36. Stewart, E.; Newman, J.; Tikoff, B.; Donnelly, S.; German, L.; Chatzaras, V.; Lamb, W.; Miller, B.; Kruckenberg, S. Coupled deformation and melt-migration events recording subduction initiation, Dun Mountain ophiolite, New Zealand. *Geol. Soc. Lond. Mem.* **2019**, *49*, 93–117. [CrossRef]
37. Johnston, M. *Sheet O27AC Dun Mountain, Geological Map of New Zealand 1: 50 000: Map (1 Sheet) and Notes (40p)*; New Zealand Department of Scientific and Industrial Research: Nelson, New Zealand, 1981.
38. Sano, S.; Tazaki, K.; Koide, Y.; Nagao, T.; Watanabe, T.; Kawachi, Y. Geochemistry of dike rocks in Dun mountain ophiolite, Nelson, New Zealand. *N. Z. J. Geol. Geophys.* **1997**, *40*, 127–136. [CrossRef]
39. Webber, C.; Little, T.; Newman, J.; Tikoff, B. Fabric superposition in upper mantle peridotite, Red Hills, New Zealand. *J. Struct. Geol.* **2008**, *30*, 1412–1428. [CrossRef]
40. Webber, C.; Newman, J.; Holyoke, C.; Little, T.; Tikoff, B. Fabric development in cm-scale shear zones in ultramafic rocks, Red Hills, New Zealand. *Tectonophysics* **2010**, *489*, 55–75. [CrossRef]
41. Kimura, J.; Sano, S. Reactive Melt Flow as the Origin of Residual Mantle Lithologies and Basalt Chemistries in Mid-Ocean Ridges: Implications from the Red Hills Peridotite, New Zealand. *J. Petrol.* **2012**, *53*, 1637–1671. [CrossRef]
42. Walcott, R. Geology of the Red Hill Complex, Nelson, New Zealand. *Trans. R. Soc. N. Z. Earth Sci.* **1969**, *7*, 57–88.
43. Chatzaras, V.; Kruckenberg, S.; Cohen, S.; Medaris, L.; Withers, A.; Bagley, B. Axial-type olivine crystallographic preferred orientations: The effect of strain geometry on mantle texture. *J. Geophys. Res. Solid Earth* **2016**, *121*, 4895–4922. [CrossRef]
44. Lloyd, G. Atomic number and crystallographic contrast images with the SEM: A review of backscattered electron techniques. *Mineral. Mag.* **1987**, *51*, 3–19. [CrossRef]
45. Bestmann, M.; Prior, D. Intragranular dynamic recrystallization in naturally deformed calcite marble: Diffusion accommodated grain boundary sliding as a result of subgrain rotation recrystallization. *J. Struct. Geol.* **2003**, *25*, 1597–1613. [CrossRef]
46. Suwas, S.; Ray, R. *Crystallographic Texture of Materials*; Springer: London, UK, 2014.
47. Wright, S.; Nowell, M.; Field, D. A review of strain analysis using electron backscatter diffraction. *Microsc. Microanal.* **2011**, *17*, 316–329. [CrossRef] [PubMed]
48. Hielscher, R.; Schaeben, H. A novel pole figure inversion method: Specification of the MTEX algorithm. *J. Appl. Crystallogr.* **2008**, *41*, 1024–1037. [CrossRef]
49. Bachmann, F.; Hielscher, R.; Schaeben, H. Grain detection from 2d and 3d EBSD data–specification of the MTEX algorithm. *Ultramicroscopy* **2011**, *111*, 1720–1733. [CrossRef]
50. Bachmann, F.; Hielscher, R.; Schaeben, H. Texture analysis with MTEX–free and open source software toolbox. *Solid State Phenom.* **2010**, *160*, 63–68. [CrossRef]
51. Skemer, P.; Katayama, I.; Jiang, Z.; Karato, S. The misorientation index: Development of a new method for calculating the strength of lattice-preferred orientation. *Tectonophysics* **2005**, *411*, 157–167. [CrossRef]
52. Woodcock, N. Specification of fabric shapes using an eigenvalue method. *Geol. Soc. Am. Bull.* **1977**, *88*, 1231–1236. [CrossRef]
53. Vollmer, F. An application of eigenvalue methods to structural domain analysis. *Geol. Soc. Am. Bull.* **1990**, *102*, 786–791. [CrossRef]
54. Mainprice, D.; Bachmann, F.; Hielscher, R.; Schaeben, H. Descriptive tools for the analysis of texture projects with large datasets using MTEX: Strength, symmetry and components. *Geol. Soc. Lond. Spec. Publ.* **2014**, *409*, 251–271. [CrossRef]
55. Ulrich, S.; Mainprice, D. Does cation ordering in omphacite influence development of lattice-preferred orientation? *J. Struct. Geol.* **2005**, *27*, 419–431. [CrossRef]
56. Jung, H.; Karato, S. Water-Induced Fabric Transitions in Olivine. *Science* **2001**, *293*, 1460–1464. [CrossRef] [PubMed]
57. Michibayashi, K.; Oohara, T. Olivine fabric evolution in a hydrated ductile shear zone at the Moho Transition Zone, Oman Ophiolite. *Earth Planet. Sci. Lett.* **2013**, *377–378*, 299–310. [CrossRef]
58. Michibayashi, K.; Mainprice, D.; Fujii, A.; Uehara, S.; Shinkai, Y.; Kondo, Y.; Ohara, Y.; Ishii, T.; Fryer, P.; Bloomer, S.H.; et al. Natural olivine crystal-fabrics in the western Pacific convergence region: A new method to identify fabric type. *Earth Planet. Sci. Lett.* **2016**, *443*, 70–80. [CrossRef]
59. Baptiste, V.; Tommasi, A.; Vauchez, A.; Demouchy, S.; Rudnick, R.L. Deformation, hydration, and anisotropy of the lithospheric mantle in an active rift: Constraints from mantle xenoliths from the North Tanzanian Divergence of the East African Rift. *Tectonophysics* **2015**, *639*, 34–55. [CrossRef]
60. Zhang, S.; Karato, S.; Gerald, J.; Faul, U.; Zhou, Y. Simple shear deformation of olivine aggregates. *Tectonophysics* **2000**, *316*, 133–152. [CrossRef]

61. Ramsay, J.G. Development of chevron folds. *Geol. Soc. Am. Bull.* **1974**, *85*, 1741–1754. [CrossRef]
62. Soustelle, V.; Tommasi, A.; Bodinier, J.; Garrido, C.; Vauchez, A. Deformation and Reactive Melt Transport in the Mantle Lithosphere above a Large-scale Partial Melting Domain: The Ronda Peridotite Massif, Southern Spain. *J. Petrol.* **2009**, *50*, 1235–1266. [CrossRef]
63. Soustelle, V.; Tommasi, A.; Demouchy, S.; Franz, L. Melt-rock interactions, deformation, hydration and seismic properties in the sub-arc lithospheric mantle inferred from xenoliths from seamounts near Lihir, Papua New Guinea. *Tectonophysics* **2013**, *608*, 330–345. [CrossRef]
64. Tommasi, A.; Baptiste, V.; Vauchez, A.; Holtzman, B. Deformation, annealing, reactive melt percolation, and seismic anisotropy in the lithospheric mantle beneath the southeastern Ethiopian rift: Constraints from mantle xenoliths from Mega. *Tectonophysics* **2016**, *682*, 186–205. [CrossRef]
65. Miranda, E.; Hirth, G.; John, B. Microstructural evidence for the transition from dislocation creep to dislocation-accommodated grain boundary sliding in naturally deformed plagioclase. *J. Struct. Geol.* **2016**, *92*, 30–45. [CrossRef]
66. Závada, P.; Schulmann, K.; Racek, M.; Hasalová, P.; Petr, J.; Weinberg, R.; Štípská, P.; Roberts, A. Role of strain localization and melt flow on exhumation of deeply subducted continental crust. *Lithosphere* **2018**, *10*, 217–238. [CrossRef]
67. Hidas, K.; Borghini, G.; Tommasi, A.; Zanetti, A.; Rampone, E. Interplay between melt infiltration and deformation in the deep lithospheric mantle (External Liguride ophiolite, North Italy). *Lithos* **2021**, *380–381*, 105855. [CrossRef]
68. Shao, Y.; Piazolo, S.; Liu, Y.; Lee, A.; Jin, W.; Li, W.; Liang, C.; Wen, Q. Deformation Behavior and Inferred Seismic Properties of Tonalitic Migmatites at the Time of Pre-melting, Partial Melting, and Post-Solidification. *Geochem. Geophys. Geosyst.* **2021**, *22*, e2020GC009202. [CrossRef]
69. Shao, Y.; Prior, D.J.; Scott, J.M.; Negrini, M. Pre-Alpine Fault Fabrics in Mantle Xenoliths from East Otago, South Island, New Zealand: Journal of Geophysical Research. *Solid Earth* **2021**, *126*, e2020JB020196. [CrossRef]
70. Jung, H.; Katayama, I.; Jiang, Z.; Hiraga, T.; Karato, S. Effect of water and stress on the lattice-preferred orientation of olivine. *Tectonophysics* **2006**, *421*, 1–22. [CrossRef]
71. Liu, W.; Zhang, J.; Barou, F. B-type olivine fabric induced by low temperature dissolution creep during serpentinization and deformation in mantle wedge. *Tectonophysics* **2018**, *722*, 1–10. [CrossRef]
72. Miyazaki, T.; Sueyoshi, K.; Hiraga, T. Olivine crystals align during diffusion creep of Earth's upper mantle. *Nature* **2013**, *502*, 321–326. [CrossRef]
73. Précigout, J.; Hirth, G. B-type olivine fabric induced by grain boundary sliding. *Earth Planet. Sci. Lett.* **2014**, *395*, 231–240. [CrossRef]
74. Katayama, I.; Karato, S. Effect of temperature on the B- to C-type olivine fabric transition and implication for flow pattern in subduction zones. *Phys. Earth Planet. Inter.* **2006**, *157*, 33–45. [CrossRef]
75. Raterron, P.; Amiguet, E.; Chen, J.; Li, L.; Cordier, P. Experimental deformation of olivine single crystals at mantle pressures and temperatures. *Phys. Earth Planet. Inter.* **2009**, *172*, 74–83. [CrossRef]
76. van der Wal, D.; Chopra, P.; Drury, M.; Fitz Gerald, J. Relationships between dynamically recrystallized grain size and deformation conditions in experimentally deformed olivine rocks. *Geophys. Res. Lett.* **1993**, *20*, 1479–1482. [CrossRef]
77. Tommasi, A.; Tikoff, B.; Vauchez, A. Upper mantle tectonics: Three-dimensional deformation, olivine crystallographic fabrics and seismic properties. *Earth Planet. Sci. Lett.* **1999**, *168*, 173–186. [CrossRef]
78. Kumamoto, K.; Warren, J.; Hansen, L. Evolution of the Josephine Peridotite Shear Zones: 2. Influences on Olivine Cpo Evolution. *J. Geophys. Res. Solid Earth* **2019**, *124*, 12763–12781. [CrossRef]
79. Tommasi, A.; Mameri, L.; Godard, M. Textural and compositional changes in the lithospheric mantle atop the Hawaiian plume: Consequences for seismic properties. *Geochem. Geophys. Geosyst.* **2020**, *21*, e2020GC009138. [CrossRef]
80. Jung, H.; Park, M.; Jung, S.; Lee, J. Lattice preferred orientation, water content, and seismic anisotropy of orthopyroxene. *J. Earth Sci.* **2010**, *21*, 555–568. [CrossRef]
81. Zaffarana, C.; Tommasi, A.; Vauchez, A.; Grégoire, M. Microstructures and seismic properties of south Patagonian mantle xenoliths (Gobernador Gregores and Pali Aike). *Tectonophysics* **2014**, *621*, 175–197. [CrossRef]
82. Fernández-Roig, M.; Galán, G.; Mariani, E. Deformation and seismic anisotropy of the subcontinental lithospheric mantle in NE Spain: EBSD data on xenoliths from the Catalan Volcanic Zone. *Tectonophysics* **2017**, *698*, 16–37. [CrossRef]

Disclaimer/Publisher's Note: The statements, opinions and data contained in all publications are solely those of the individual author(s) and contributor(s) and not of MDPI and/or the editor(s). MDPI and/or the editor(s) disclaim responsibility for any injury to people or property resulting from any ideas, methods, instructions or products referred to in the content.